5-2017

Aluminum Multicharged Ion Generation from Femtosecond Laser Plasma

Md. Haider A. Shaim
Old Dominion University

Frederick Guy Wilson
Old Dominion University

Hani E. Elsayed-Ali
Old Dominion University, helsayed@odu.edu

Aluminum multicharged ion generation from femtosecond laser plasma

Md. Haider A. Shaim, Frederick Guy Wilson, and Hani E. Elsayed-Ali[a]
Department of Electrical and Computer Engineering and the Applied Research Center, Old Dominion University, Norfolk, Virginia 23529, USA

Aluminum multicharged ion generation from femtosecond laser ablation is studied. A Ti:sapphire laser (wavelength 800 nm, pulse width $\sim$100 fs, and maximum laser fluence of 7.6 J/cm^2) is used. Ion yield and energy distribution of each charge state are measured. A linear relationship between the ion charge state and the equivalent acceleration energy of the individual ion species is observed and is attributed to the presence of an electric field within the plasma-vacuum boundary that accelerates the ions. The ion energy distribution follows a shifted Coulomb-Boltzmann distribution. For Al^{1+} and Al^{2+}, the ion energy distributions have two components; the faster one can be attributed to multiphoton laser ionization, while the slower one is possibly due to collisional processes. Ion extraction from the plasma is increased with an applied external electric field, which is interpreted to be due to the retrograde motion of the plasma edge as a result of the external electric field. Multicharged ion generation by femtosecond laser ablation is compared to previously reported ion generation with nanosecond laser ablation and is shown to require significantly lower laser fluence and generates higher charge states and more energetic ions. *Published by AIP Publishing.*
[http://dx.doi.org/10.1063/1.4983008]

I. INTRODUCTION

Multicharged ion (MCI) sources are of interest as a tool for nanoprocessing and nanofabrication. The total energy of an ion depends on its charge state (potential energy) and velocity (kinetic energy). MCI sources are being developed for utilization in surface modification (e.g., etching and deposition), for ion implantation, and for fundamental studies of ion-surface interactions.[1] For MCIs, the requirement on the high voltage power supply is reduced since ions are accelerated by an electric field to an energy that is proportional to their charge. This makes it possible to develop comparatively low-cost and compact ion sources.

Pulsed laser ablation of a solid target can be used to generate ions with different charges from a variety of target materials. The laser-ablated plasma can be considered as an instantaneous ion point source with the characteristic ion emission time smaller than the ion drift time and the plasma plume dimension much smaller than the source-to-ion collector distance.[2] Pulsed laser interaction with a solid is initiated by the absorption of part of the incident laser pulse causing target heating, melting, vaporization, ionization, particle ejection, and plasma formation and expansion. The laser pulse width, wavelength, and pulse energy density determine the heat-affected zone, the ablation mechanism, plasma properties, and plasma expansion dynamics.[3,4] Dense plasma consisting of electrons, ions, clusters, and neutrals is generated due to the laser-matter interaction. The interaction of a high power density laser pulse with the target results in the ablation of the target surface. When the femtosecond laser intensity is 10^{13}–10^{14} W/cm^2, ionization of the target material, occurring during the initial laser-solid interaction, is the dominant

mechanism.[5] After the initial ionization by inverse bremsstrahlung and resonant absorption, electron-photon energy transfer takes place between the free electrons and the remaining femtosecond laser pulse.[5] During this time, a thin sheath of electrons and ions forms and begins to generate a bubble on the laser-irradiated surface. The electron cooling time ($\tau_e \sim 1$ ps) is longer than the temporal duration of the 100-fs laser pulse; therefore, the interaction of the femtosecond laser pulse with the metal target is already completed before the excited electrons transfer their energy into the lattice of the target via an electron-phonon coupling.[6] Evaporative ablation due to the energy transfer to the lattice by the electrons results in the formation of the plasma plume.

When a nanosecond laser is used to ablate a solid target, the ablation process can be divided into three main stages: evaporation of target material, interaction between the evaporated material and laser pulse resulting in the material heating and plasma formation, and plasma plume expansion and rapid cooling.[7] The main absorption mechanisms of the plasma consist of the electron-atom inverse bremsstrahlung, electron-ion inverse bremsstrahlung, photoionization, and Mie absorption.[8] The contribution of each of these mechanisms depends on the laser pulse width, the stage of plasma formation, and the plasma properties. For nanosecond laser ablation, the electrons in the plume gain energy mainly by inverse bremsstrahlung. The electrons transfer their energy to the ions and the neutrals through collisional processes. The time needed to transfer the energy from the electrons to the ions is much shorter than the nanosecond laser pulse duration resulting in the thermalization of the electrons and ions in the laser plume. Due to the small mass of the electrons compared to the ions, some of the thermalized electrons develop high velocities and escape much earlier than the ions resulting in the formation of a transient electrostatic

[a]Author to whom correspondence should be addressed. Electronic mail: helsayed@odu.edu. Telephone: (757)269-5645.

field (double-layer potential) at the expanding plasma-vacuum boundary.[9] This double-layer potential accelerates the ions according to their charge state.[10,11] As the laser pulse energy is increased, the plasma density increases as well, reaching a density where the plasma plume absorbs a significant part of the remaining laser pulse. In this case, the degree of plasma ionization increases producing a higher state ion charge.

In femtosecond laser ablation, the laser pulse width is shorter than the electron-phonon coupling time and the heat transport time in the solid.[6,12,13] Therefore, femtosecond laser ablation causes a smaller heat affected zone compared to nanosecond ablation.[14] For laser intensities significantly higher than the ablation threshold, as is the case for MCI generation, ablation proceeds mainly by thermal vaporization.[15,16] In femtosecond laser ablation, plasma expansion occurs after absorption of the laser pulse.

Several groups reported on ion emission by femtosecond laser pulse irradiation of a solid target.[4,17–19] Using a Ti:sapphire laser (wavelength $\lambda = 800$ nm, pulse width $\tau = 60$ fs, and laser fluence $F = 8.5$ J/cm^2), Irimicuic et al. performed Langmuir probe measurement on transient plasmas from several metallic targets. The time-of-flight (TOF) profile of the ion current was fitted to a shifted Maxwell-Boltzmann velocity distribution and used to reconstruct the probe I–V characteristics. This technique allowed for obtaining the temporal development of the ion and electron temperatures and densities, up to 10 μs after the laser pulse.[4] For an Al target, the electron temperature was ~1.6 eV measured 8 μs after the laser pulse, while the ion temperature, determined from the shifted Maxwell-Boltzmann fit of the probe ion signal, was ~3 eV. Anoop et al. used spatially and temporally resolved optical emission spectroscopy of the laser plume to study the dynamics of ions and neutrals generated by ablating Cu using a Ti:sapphire laser ($\lambda = 800$ nm, and $\tau = 40$ fs, and $F = 0.5$–77.5 J/cm^2). For $F > 10$ J/cm^2, splitting of the plasma plume is observed and was attributed to the fast moving ions separating from the slow neutrals. For $F > 50$ J/cm^2, the maximum energy estimated for the ions and neutrals was ~800 and ~30 eV, respectively.[17] Their imaging results were correlated to Faraday cup (FC) and Langmuir probe measurements of the charged particles. Kelley et al. used a Faraday cup to study the plasma from C, Al, and Cu targets ablated by a Ti:sapphire laser ($\lambda = 800$ nm, $\tau = 70$ fs, and $F = 0.1$–1 J/cm^2).[18] They reported a bi-modal ion kinetic energy distribution with the lower distribution following the shifted Maxwell-Boltzmann, attributed to thermal ionization, whereas the higher distribution was non-Maxwellian, attributed to space-charge effects within the plume.[18] Donnelly et al. studied the expansion dynamics and the various plume components in laser ablation ($\lambda = 527$ nm, $\tau = 250$ fs, and maximum $F \sim 0.8$ J/cm^2) of a Ni target. Ion TOF profiles and thickness map of deposition on a transparent substrate were obtained. The ion energy normal to target was ~35 and ~100 eV for laser fluences of ~0.1 and ~0.8 J/cm^2, respectively.[19]

Generation of energetic MCIs by femtosecond laser pulse irradiation of a solid target with moderate powers was previously reported.[20–22] Gordienko et al. generated up to Si^{12+} by ablation of a Si target with a femtosecond dye-laser

($\lambda = 616$ nm, $\tau = 200$ fs, and maximum intensity $I = 3 \times 10^{16}$ W/cm^2).[20] The surface of the Si target was cleaned by ablating it with a nanosecond laser pulse of fluence 3 J/cm^2 prior to femtosecond laser ablation. Fast and slow components of the Si ions were observed; the fast ions gain energy according to their charge state, while for the slow ions, the energy gain increases with the charge state. This was explained by recombination that occurs at a faster rate for the slower ions since slower ions spend more time to reach the detector.[20] In that experiment, the residual gas pressure was $\leq 2 \times 10^{-5}$ Torr.[20] Zheng et al. used a Langmuir probe and an electrostatic ion energy analyzer to study the Al plasma characteristics generated by a nanosecond Nd:YAG laser ($\lambda = 1064$ nm, $\tau = 6$ ns, and $F = 1.3$ J/cm^2) and a femtosecond Ti:sapphire laser ($\lambda = 780$ nm, $\tau = 100$ fs, and $F = 0.4$ J/cm^2). The maximum charge state achieved by the nanosecond and femtosecond lasers was Al^{2+} and Al^{3+}, respectively.[21] The plasma characteristics generated by these two lasers were studied for comparable ablation flux using a Langmuir probe and an ion energy analyzer. The nanosecond laser pulse produced a greater concentration of low energy and low charge state ions compared to the femtosecond laser. Chutko et al. used an ion energy/charge cylindrical analyzer combined with the TOF analysis to study the ion generation from the ablation of Si by a femtosecond laser ($\lambda = 616$ nm, $\tau = 200$ fs, and $I \leq 2 \times 10^{16}$ W/cm^2).[22] Generation of charge states up to Si^{6+}, O^{4+}, and C^{6+} was reported. The O and C ions were attributed to impurities on the Si surface.

We report on aluminum MCI generation by a Ti:sapphire femtosecond laser ($\lambda = 800$ nm, $\tau \sim 100$ fs, $F \leq 7.6$ J/cm^2) ablation without and with ion acceleration in an external electric field between the target and a grounded mesh. The velocity and the charge state of the MCIs are determined by using ion TOF and electrostatic retarding field ion energy analyzer. The electric field generated in the plume-vacuum interface that is responsible for the ion acceleration is estimated from the deconvolution of the ion pulse into individual ion species. Distinct higher order charge states along with the increase in the total number of ions generated are observed with the increase in the laser pulse energy. Ions up to Al^{6+} were observed. These results are compared to our earlier nanosecond Al MCI generation using a Q-switched Nd:YAG laser (wavelength $\lambda = 1064$ nm, pulse width $\tau \sim 7$ ns, and fluence $F \leq 38$ J/cm^2).[23,24] The extracted MCIs from the femtosecond laser ablation gain more energy from the external electric field compared to nanosecond ablation due to the lower plasma shielding effect in the femtosecond case.

II. EXPERIMENTAL

A Spectra-Physics femtosecond amplified Ti:sapphire laser is used to ablate the Al target. The laser produces ~100 fs (measured with a single shot auto-correlator) laser pulses at 800 nm with a repetition rate of 1 kHz and a laser fluence up to 7.6 J/cm^2. The ions are generated in a vacuum chamber where the femtosecond laser irradiates the Al target. The generated ions are then accelerated towards the Faraday cup (FC) through a drift tube. The diameter of the ion generation chamber is 30 cm. A 125 cm long transport tube with an
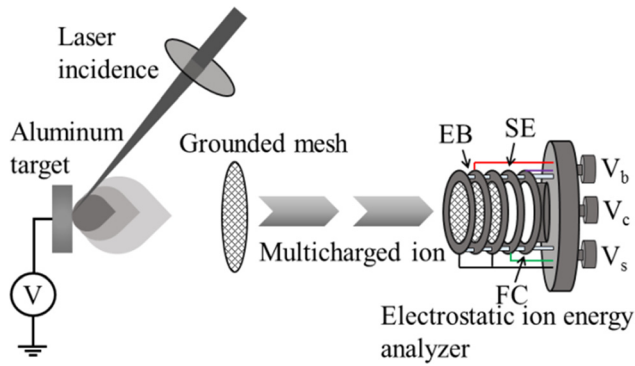
FIG. 1. An illustration of the laser MCI ion source showing the laser irradiating the Al target and the electrostatic TOF energy analyzer. EB is the electrostatic barrier electrode, SE suppressor electrode, and FC Faraday cup.

inner diameter of 10 cm is connected to the chamber. An illustration of the MCI source is shown in Fig. 1.

The Al target ($\sim$1 cm square, 0.5 mm thick, 99.97% pure Al foil) was placed on a multi-axis translational stage. The laser beam is focused on the Al target surface at an angle of 45° with the surface using a lens of 32-cm focal length positioned on a horizontal translation stage. The laser spot area at focus was $\sim$8 $\times$ 10^{-5} cm^2, as obtained using the knife-edge method at the target-equivalent plane with the edge scanned at 45° to the laser beam. The Al target support is placed inside the MCI generating chamber using an insulated connector. This arrangement allows for applying an accelerating voltage directly to the Al target while keeping the experimental chamber at ground. The femtosecond laser pulses pass to the Al target through a viewport which has $\sim$8% loss in optical power due to Fresnel reflections. For ion extraction, a nickel mesh of diameter 10-cm, thickness of 100 μm, and with an open area of 70% is placed 15-cm in front of the target. The generated ions are accelerated in the gap between the Al target and the extraction mesh. The ions are accelerated by the combined effect of the expanding plasma, the electric field developed in the plasma-vacuum interface due to double-layer formation,[23] and the external applied electric field. After passing the extraction mesh, the ions drift in the transport tube with a constant velocity. The MCIs are detected at the end of the transport tube using an Al Faraday cup (FC) with a diameter of 5 cm. To suppress the secondary electrons from the FC due to positive ion collisions, the suppressor electrode ring, located 1 cm before the FC, is biased with -140 V.[25] Throughout the experiment, the FC voltage was maintained at -70 V. The retarding field ion energy analyzer consists of three nickel meshes, similar to the extraction mesh but with a diameter of 5 cm, each separated by 1 cm and placed with the closest mesh to target at a distance of 130 cm away from the Al target. To analyze the ion energy distribution, a variable voltage is applied to the electrostatic barrier (EB) electrode, which is the central electrode of the three-grid retarding field analyzer. The 1-kHz femtosecond laser pulses are gated by a fast mechanical shutter to select only a single laser pulse that irradiates the Al target. The oscilloscope is triggered by a fast photodiode detector observing the optical leak in the last mirror before the focusing lens. Inside the vacuum chamber, the loss of

MCIs by charge transfer with the background gas is negligible under our experimental conditions (background gas in the UHV chamber is in the low 10^{-9} Torr). The total scattering cross section for ions with different charge states was previously measured.[26–28] The mean free path of the Al ions depends on their charge state, but for background pressures as in our vacuum chamber is $\gtrsim$10 km for Al ions up to 6+. As the travel distance of the ions from the target to the Faraday cup is 1.4 m, ion recombination in the drift tube is negligible.

III. RESULT AND DISCUSSION

The ion signal recorded on the oscilloscope from the FC was analyzed using Origin Pro version 9.1 software to determine the total charge of the Al ions delivered to the FC. Origin software allows processing the data recorded by the oscilloscope using a Fast Fourier Transform filter with a 5-point window in order to filter and smooth noise in the measured signal. The total charge delivered to the FC Q_i is given by $Q_i = \frac{1}{R_L} \int V_F(t) dt$, where $V_F(t)$ is the voltage signal detected by the FC and R_L is the 50 Ω internal resistance of the oscilloscope.

To observe the effect of consecutive laser pulses hitting the same spot on the target, we calculated the total ion generation per pulse for each laser pulse starting with a fresh target surface area. The femtosecond laser pulse fluence of 7.6 J/cm^2 was focused on the surface of the Al target. The ion signal was observed, and the number of ions produced was calculated for an accelerating voltage of 0–6 kV. The general behavior of the number of ions detected with consecutive laser pulses is that it increases after the first or second laser pulse, due to surface cleaning, followed by a slight reduction with laser pulses interacting with the same surface area due to drilling of the target. For the laser conditions used, the highest ion yield occurs at the 3rd laser pulse. Although there are pulse-to-pulse fluctuations in the magnitude of the ion signal due to a certain charge, the ion energy and energy distribution, as detected by TOF, remains consistent. For example, the peak amplitude of Al^{1+} was observed to fluctuate by 23% over four consecutive laser pulses, while the TOF of the ions, which is indicative of ion energy, remained almost unchanged. The reported data are collected for the 3rd pulse to avoid the effect of any oxide or contaminants on the surface of the Al target. A different target spot was used for each data point, and each target spot was located at least 1 mm radially from the previous one, so that no two spots overlap. The voltage on target was measured with a fast high voltage probe.

A. Ions detected without external acceleration

The interaction of the femtosecond laser pulse with the surface of the target creates dense hot plasma within the time scale of the laser pulse. Subsequently, the plasma expands adiabatically into the vacuum. In the plume, the ion kinetic energy can range from hundreds of eV to several keV depending on the laser fluence.[22] The plume expansion is mainly perpendicular to the sample surface. To characterize the generated ions from the laser plasma without applying

accelerating voltage to the target, the voltage bias on the electrostatic barrier (EB) was incrementally increased from 0 V to a voltage that resulted in complete suppression of the ions detected. Fig. 2 shows the TOF spectrum for 0, 50, 100, 200, and 325 V positive voltages applied to the EB. The laser fluence of 7.6 J/cm^2 was used to ablate the Al target. The plasma ion peak drifts towards the FC with a velocity of $\sim 3.8 \times 10^4$ ms^{-1} when no barrier voltage is applied. The inset of Fig. 2 shows the reduction in the total number of charge reaching the FC with the increase in the electrostatic barrier voltage. The ion bunch generated by pulsed laser ablation that reaches the FC contains different ionic states. The double-layer potential, developed in the laser-generated plasma plume, at the plasma vacuum interface, accelerates the ions.[9] Higher charge state ions reach the FC earlier than those with a lower charge since the ions with a higher charge gain more kinetic energy from the double-layer potential. From Fig. 2, we observe that the EB bias of ~ 325 V stops most ($\sim 95\%$) of the Al ions generated.

Many factors affect the ion energy: most importantly, plasma temperature, adiabatic expansion of the plasma plume, and Coulomb acceleration due to the double-layer potential at the plasma-vacuum interface of the expanding plume.[9,29] The emitted ion charge states are identified from their TOF signal. Also, the ion energy distribution is obtained from the retarding energy analyzer and from the TOF signal. Therefore, deconvolution of the TOF signal into individual ion charge signals can be accomplished based on the assumption of local thermodynamic equilibrium (LTE) in the expanding laser plume.[29] The velocity distributions of the laser ablated ions far from the irradiated target, where the ion charge-states are frozen, are characterized by a shifted Coulomb-Boltzmann (SCB) distribution for each ion species. This SCB distribution is given as[29,30]

$$F(v) = A_0 \left(\frac{m}{2\pi kT} \right)^{\frac{3}{2}} (v)^3 \exp\left[-\frac{m}{2kT} (v - v_k - v_c)^2 \right], \quad (1)$$

where $v = v_t + v_k + v_c$ denotes the total velocity along the normal to the target surface, v_t is the mean thermal velocity for monoatomic neutral species, v_k is the adiabatic

FIG. 2. Ion signal detected by the FC for various EB voltage biases at the laser fluence of 7.6 J/cm^2. Inset shows the reduction of total charge with the increase of barrier voltage when no accelerating voltage is applied to the target.

expansion velocity, v_c is the velocity due to Coulomb acceleration, and A_0 is a normalization constant. These velocities are obtained from the following:

$$v_t = \sqrt{\left(\frac{3kT}{m} \right)}; \quad v_k = \sqrt{\left(\frac{\Upsilon kT}{m} \right)}; \quad v_c = \sqrt{\left(\frac{2ze V_0}{m} \right)},$$

where m is the mass of ablated ion, Υ is the adiabatic coefficient which, for a monoatomic metal, e.g., aluminum, has the value of 5/3, z is the charge state, kT is the equivalent ion plasma temperature (in eV), and V_0 is the equivalent accelerating voltage developed inside the plasma. In Eq. (1), the condition of LTE ($T_i \sim T_e \sim T$) is assumed. For a transient plasma, such as in laser-plasma, the LTE condition requires that electron-atom and electron-ion collisions are faster than radiative processes. These collisions establish equilibrium with particle velocities in the plasma following a Maxwell-Boltzmann distribution.[31,32] The validity of LTE for the laser plasma was previously considered for femtosecond laser ($\lambda = 800$ nm, $\tau = 100$ fs, and $F = 0.9 - 18$ J/cm^2) ablation,[33] which is nearly the same laser conditions used in our present experiment.

The Kelley and Dreyfus function, expressing the ion current based on the SCB distribution including the effect of Coulomb energy in terms of an equivalent accelerating voltage, can be applied for the analysis of the ion current if the TOF of ions is much longer than the duration of the laser pulse.[34,35] The SCB model considers both thermal and Coulomb interactions. TOF signal of each ion species can be written as $F(t) = F(v)\frac{dv}{dt}$, where $F(v)$ is given in Eq. (1). Therefore, the overall distribution of the ejected ions is a sum of individual SCB distributions with their characteristics equivalent accelerating voltage and ion plasma temperature

$$F(t) = \sum_i A_i \left(\frac{m}{2\pi kT} \right)^{\frac{3}{2}} \left(\frac{L^4}{t^5} \right)$$
$$\times \exp\left[-\frac{m}{2kT} \left(\frac{L}{t} - \sqrt{\frac{\Upsilon kT}{m}} - \sqrt{\frac{2ze V_0}{m}} \right)^2 \right]. \quad (2)$$

In Eq. (2), A_i are normalization constants, t is the time-of-flight, and L is the total distance from the target to the Faraday cup.[36] Eq. (2) applies under the condition of absence of significant recombination and collisional excitation processes; i.e., ion species are frozen and freely drifting in the vacuum. Such properties were observed for an expanding laser plasma outside the recombination zone.[37] The parameters used to fit the TOF ion signal with Eq. (2) are mostly sensitive to the equivalent ion plasma temperature kT and the equivalent acceleration voltage V_0 developed in the plume due to the double-layer potential formed at the plasma-vacuum interface. From this fit of the measured TOF signal with Eq. (2), we can estimate kT and V_0.

The ion pulse detected by the FC, shown in Fig. 2, consists of ions with different charge states. In order to determine the contribution of each ion charge to the TOF signal, deconvolution of the ion pulse signal for each ion charge state is performed. To obtain the best fit to the TOF signal, a
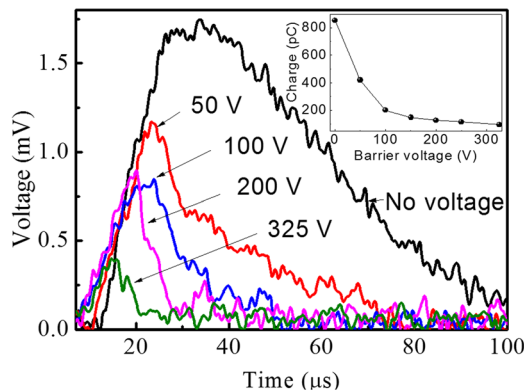
combination kT and V_0 is used. These two parameters are used to estimate the effects of thermal, adiabatic, and Coulomb potential on the different ion charges. The deconvolution of the ion pulse into different ion charges is conducted as follows: (1) The ion energy distribution of each charge state is assumed to follow the SCB distribution described in Eq. (1); (2) the maximum charge state z generated is based on the TOF measurement conducted by separating the charge states temporally using an externally applied electric field between the target and the grounded mesh, as discussed in Section III B; (3) the equivalent accelerating voltage developed inside the plasma due to the double-layer potential V_0 and the equivalent ion plasma temperature kT are set as free variables conditional upon the total energy (sum of thermal, adiabatic, and Coulomb) matching with the ion energy measured by the three-grid retarding field analyzer; (4) the most probable energy of each ion charge is separated by V_0 since the ions gain energy from V_0 that is proportional to their charge z; and (5) the sum of the TOF signal due to the different ion charges fits the TOF signal of the observed ion pulse that is composed of all ions.

In laser-generated ions, two energy distributions for Al^{1+} and Al^{2+} were reported using an Nd:YAG laser ($\lambda = 532$ nm, $\tau = 5$ ns, and $F = 0.8 - 6$ J/cm^2).[38] Also, slow and fast Si MCI generation using a femtosecond laser ($\lambda = 616$ nm, $\tau = 200$ fs, and maximum intensity $I = 3 \times 10^{16}$ W/cm^2) was reported.[20] The faster group was attributed to multiphoton laser ionization, while the slow group was attributed to collisional processes.[38] Within the expanding plume, collisions among ions, electrons, and neutrals lead to ionization, recombination, and charge transfer resulting in ions with different charge states than the source ion species. The ions are accelerated depending on their charge state and their energy, also, depends on their formation process. Therefore, a particular ion charge can have more than one independent SCB distributions.[38] The acceleration of these ions also depends on the location between the target and grounded mesh at which the ion is generated and can experience the external electric field. Plasma shielding reduces ion acceleration by the external electric field. For example, if recombination is the dominant process $(Al^{2+} + e \rightarrow Al^{1+} + h\nu)$, the Al^{2+} and Al^{1+} involved in this reaction will contribute to the energy distribution for the Al^{1+} ions. We considered slow Al^{1+} and Al^{2+} generation along with the fast ions, since multiple peak structures in the TOF signal are observed for these ion groups.

The deconvolution of the ion pulse into individual ion species, shown in Fig. 3, results in a temporal distribution of ion states throughout the ion pulse. The higher charge state ions have higher energy and reach the FC earlier than the lower charge states. The sum of the signals from different ion charges gives the total ion signal which is fitted to the experimental TOF signal. From Figs. 2 and 3, each ion charge is affected by the retarding field according to its charge state resulting in a reduction in the ion pulse amplitude at all times, throughout the ion pulse, due to the temporal separation of the different ion charges. From the deconvolution, we recover charge states up to Al^{6+}. This is confirmed by the individual ion charge signals observed after separation of the different
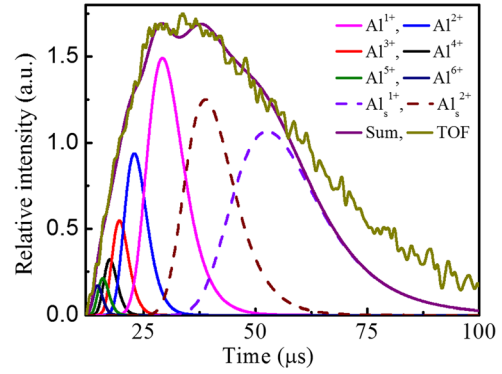

FIG. 3. Deconvolution of TOF spectrum into individual ion species for the laser fluence of 7.6 J/cm^2 when no accelerating voltage is applied to target. Al_s^{1+} and Al_s^{2+} are the slower ions.

ion charges with a voltage applied on the target making it possible to identify each by their time-of-flight.

The curve fit for the extracted Al ions in Fig. 3 was done for $V_0 = 250$ V and $kT = 25$ eV for the fast ions. For the slow Al^{1+} and Al^{2+} ions, $V_0 = 90$ V and $kT = 18$ eV. The stretched tail of the ion pulse indicates the possibility of more groups of slow ions. The total energy of the Al ions without externally applied electric field is $E_{zT} = (E_t + E_k) + zE_C$, where E_{zT} is the total energy gain for charge state z, $E_t = \frac{3}{2}kT$ is the thermal energy, $E_k = \frac{\gamma}{2}kT$ is the adiabatic energy, and $E_c = eV_0$ is the Coulomb energy associated with the equivalent accelerating voltage due to the double-layer potential. In Fig. 3, the most probable energy of different ion species is separated by ~ 250 eV. The calculated most probable energy of the TOF signal and the adiabatic and thermal energy obtained by the deconvolution are in good qualitative agreement with the results found for ablation using femtosecond lasers.[39–41]

The sensitivity of the ion signals for each charge state, obtained by the deconvolution process, is checked by performing the fit to the detected TOF signal using different values of z, V_0, and kT. The maximum ion charge z is experimentally known from the TOF signal with the external accelerating field because the ions with different charges are temporally well separated. In performing the deconvolution, the sum of the ion signals of all charges detected is fitted to the measured TOF signal. This fit is best at time scales extending from the onset of the fast ions detected by the FC and extends past the peak of the TOF signal. The slower ions forming the tail of the TOF signal are not as well fitted to the SCB distribution, representing the sum of the ion charges. This is because there are secondary mechanisms forming these slower ions, as was previously discussed.[20,38] The ion pulse width for each charge state gives the value of kT. Higher kT results in a wider ion pulse for each charge state. The Coulomb energy associated with V_0 determines the ion pulse energy shift, with higher V_0 corresponds to an increased ion energy shift of the SCB distribution. The fit is more sensitive to changes in V_0 compared to changes in kT, with changes in V_0 affecting the higher charge states more profoundly. Sensitivity to fitting parameters is discussed in Section III B for ion extraction with an external electric field.

B. Ions detected with external acceleration

Since Al^{1+} has the lowest velocity among the Al ions with different charge states, the Al^{1+} ions have the longest TOF. The effective accelerating potential that the Al^{1+} experience is obtained by calculating the accelerating potential required to achieve this TOF for Al^{1+}. This potential is then used to determine the TOF of ions with other charge states. The estimated TOF for MCIs with different charge states matches the TOF signal well.

When an external electric field is present, the ions experience the double-layer potential plus the external field. The extent of which the ions experience the external field depends on the distance away from the target that they are separated from the shielding plasma. We, therefore, can extend the SCB distribution for an applied external field by adding the effective external field potential to the double-layer potential. A modified Eq. (2) is used to fit the extracted ion TOF signal, which also follows the SCB distribution, by replacing the term V_0 with total accelerating voltage $(V_0 + V_{eff})$, where V_{eff} is the effective voltage that accelerates the ions by the external field. For the extracted ions, the total accelerating energy is equal to the sum of accelerating voltage developed inside the plasma and the effective external accelerating voltage. To obtain the best fit to the TOF signal, a combination of kT and $(V_0 + V_{eff})$ is used. This analysis results in temporally separating the TOF signal into different peak positions, each corresponding to a different charge state. The signal observed by the FC is the sum of these separated ion signals. By deconvolving the TOF signal, it is possible to obtain the energy distribution for each ion charge state. Integrating over the signal from a certain charge state and dividing the integral by the 50 Ω internal resistance of the oscilloscope give the total charge for that charge state delivered to the FC. The energy distribution for each charge state is calculated from the selected peak position. The peak position of temporally separated ions, as observed from the TOF signal, can also be used. These two approaches give almost similar energy distribution for each charge state. The most probable energy of each charge state is calculated from the TOF signal.

The thermal interactions, the adiabatic expansion, and the Coulomb interactions are responsible for the ion acceleration during the plasma plume expansion.[42] In our geometry, plasma plume expansion occurs in a region with external electric field. Applying an electric field between the target and the grounded mesh accelerates the ions according to their charge state causing them to separate and, therefore, can be identified from the TOF signal collected by the FC. The ions are not accelerated to the full potential applied between the target and the grid due to plasma shielding prior to ion separation from the plume. If plasma shielding is not considered, an ion generated at the target with zero energy would reach the FC after a TOF of $t = t_a + t_d = \sqrt{\frac{2m}{zeV}}d + \sqrt{\frac{m}{2zeV}}S$, where t is the time taken by the ion to travel from target to the FC, t_a is the time that an ion is accelerated from zero velocity at target to velocity v at the extraction mesh, t_d is the time that an ion drifts at constant velocity v from the extraction mesh to the FC, d is

the distance from the target to the extraction mesh, S is the distance from the extraction mesh to the FC, m is the mass of the Al atom, e is the electron charge, z is the charge state, and V is the applied accelerating voltage. The above equation for TOF does not account for the ion acceleration in the expanding plume, which is mainly due to acceleration by the double-layer potential, the adiabatic and thermal velocity, and the effect of plasma shielding limiting the ion acceleration by the external electric field. The ion accelerating time t_a is small compared to the ion drift time t_d.

Figs. 4(a) and 4(b) show the ion signal for the accelerating voltage of 5 and 6 kV, respectively, using a laser fluence of 7.6 J/cm^2. Due to plasma shielding, the electric field established between the Al target and the grounded mesh does not fully penetrate the plasma plume resulting in ion energies less than the potential applied to the target. In Fig. 4(a), for Al^{1+}, we detect ~ 0.3 nC with most probable energy $E_{mp} \sim 2.4$ keV; for $Al^{2+} \sim 0.12$ nC with $E_{mp} \sim 4.7$ keV; for $Al^{3+} \sim 0.08$ nC of with $E_{mp} \sim 7$ keV; for $Al^{4+} \sim 0.08$ nC with $E_{mp} \sim 9.2$ keV; for $Al^{5+} \sim 0.006$ nC with $E_{mp} \sim 11.5$ keV; and for Al^{6+} 0.06 nC with $E_{mp} \sim 13.7$ keV. The peak ion energies are separated by ~ 2.3 keV for 5 kV applied to target, while for 6 kV applied to target, the peak ion energy separation increases to ~ 2.6 keV. The total energy of the ion with charge-state z when the external accelerating electric field is applied $E_{z-Total} = E_T + E_K + zE_c + zE_{eff}$, where E_{eff} is the effective acceleration energy experienced by the ion from the external electric field after considering plasma shielding. The deconvolution in Figs. 4(a) and 4(b) are fitted for the total accelerating voltage $(V_0 + V_{eff})$ of ~ 2.3 and ~ 2.6 kV and $kT \sim 40$ and ~ 45 eV, respectively. Figs. 4(a) and 4(b) also show the presence of slow Al^{1+} and Al^{2+}. In Fig. 4(a), the TOF signal for the slow ions was fitted for $(V_0 + V_{eff}) \sim 1100$ V for Al^{1+} and ~ 1900 V for Al^{2+} with $kT \sim 25$ eV, while in Fig. 4(b), slow Al^{1+} and Al^{2+} experience $(V_0 + V_{eff})$ of ~ 1300 and ~ 2100 V, respectively, with $kT \sim 30$ eV. In Figs. 4(a) and 4(b), the shoulders present at ~ 15 and ~ 14 μs in the TOF signal indicate the possibility that more slow ions contribute to the TOF signal.

The same deconvolution procedure is applied when the target is biased at a positive potential. In this case, the value of V_{eff} is adjusted to account for the external electric field. In Fig. 4(c), the fit was performed for Al^{4+} signal using different values of $(V_0 + V_{eff})$ and of kT. For a fixed kT, $(V_0 + V_{eff})$ determines the energy shift in the SCB distribution. Whereas, for a fixed $(V_0 + V_{eff})$, kT mainly determines the ion pulse width. Changing kT has a small effect on $(E_t + E_k)$ that is negligible compared to the effect of changing the accelerating potential $(V_0 + V_{eff})$. The effect of $(E_t + E_k)$ on the ion signal is constant irrespective of ion charge state. As shown in Fig. 4(c), changes in the value of $(V_{0,} + V_{eff})$ by 300 V shift the Al^{4+} ion most probable energy by 1200 eV. This shift is easily noticeable. On the other hand, changes in kT by 20 eV mostly affect the ion pulse width. The accuracy of the fitting parameter $(V_0 + V_{eff})$ increases for higher ion charge states.

For a laser fluence of 7.6 J/cm^2, increasing the accelerating voltage from 1 to 6 kV increases the total charge detected from 20 to 720 pC. In the ion transport region, the main loss
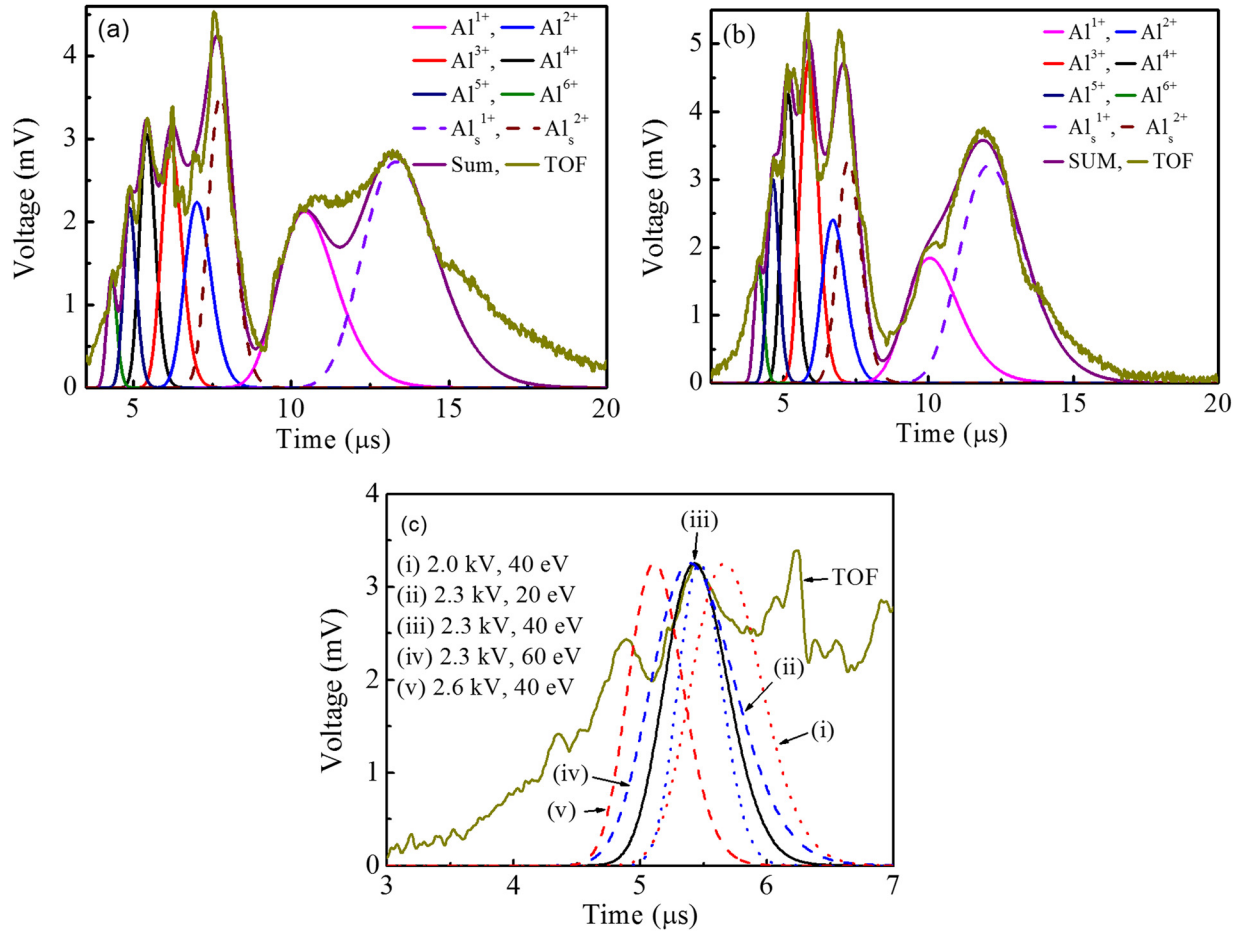
FIG. 4. Al MCI detected with (a) 5 kV and (b) 6 kV accelerating voltage. The laser fluence is 7.6 J/cm^2. The deconvolution of the extracted ion is based on a shifted Coulomb-Boltzmann distribution. (c) The effect of varying the total accelerating voltage ($V_0 + V_{eff}$) and equivalent plasma temperature kT on the deconvolution of the ion pulse when 5 kV accelerating voltage is applied. In (c), the Al^{4+} ion pulse obtained by deconvolution is shown for ($V_0 + V_{eff}$) = 2300 V and kT = 40 eV (black straight line), 2300 V and 20 eV (blue dotted line), 2300 V and 60 eV (blue dashed line), 2000 V and 40 eV (red dotted line), and 2600 V and 40 eV (red dashed line).

of detected ions is due to ion divergence resulting in ions falling outside of the FC area. The retrograde motion of the plasma edge exposes more ions to the accelerating field and repels the electrons.[43] This is the main reason for the enhancement of the ion extraction with increasing electric field between the Al target and the extraction grounded mesh. The space-charge limited flow due to the retrograde motion of the plasma and the ion current introduction in the presheath affects ion extraction.[44]

C. Effect of laser fluence

In a laser produced plasma, the plasma density, temperature, ablated mass, and the ion and electron energies are affected by the laser parameters (pulse energy, intensity, and width). The laser fluence on the Al target was varied, while all other conditions kept fixed, as described in Sec. II. The voltage applied to the Al target was 5 kV. Fig. 5(a) shows the TOF spectra detected by the FC for a laser fluence from 1.4 to 7.4 J/cm^2.

From Fig. 5(a), we observe that, for a laser fluence of 1.4 J/cm^2, a very small ion signal is detected. It is not until the laser fluence is ∼2 J/cm^2 that ion peaks at 5 and 10 μs are

detected. As the laser fluence is increased, the number of ions detected is increased along with the detection of higher charge state ions. Increasing the laser fluence increases the temporal spread of the Al^{1+} ions, possibly due to the increase in the generation of slow ions. For the lower fluences of 1.4 and 2 J/cm^2, >80% of the total ion yield is Al^{1+}, while for laser fluences above 4 J/cm^2, only ∼50% of the ions are Al^{1+}. The TOF signal shows a stretched low energy tail, which becomes clear for laser fluences above 6.3 J/cm^2 probably due to the contribution of the slower ions to the TOF signal. The shape of the ion signal depends on the energy distribution of ions, which are generated by different mechanisms. Fig. 5(b) shows the total charge detected as a function of the laser fluence. In Fig. 5(b), a linear fit was applied to determine the threshold fluence for detecting Al ions. The point at which the fitted curve intersects with the x-axis indicates that the laser fluence threshold for Al ion detection is 1.6 J/cm^2. For longer laser pulses (picosecond and nanosecond, depending of the thermal diffusivity of the target), thermal diffusion determines the ablation depth, whereas for femtosecond laser ablation both the optical penetration depth and the mean free path of nonequilibrium carriers (electrons of phonons, depending on the material) play
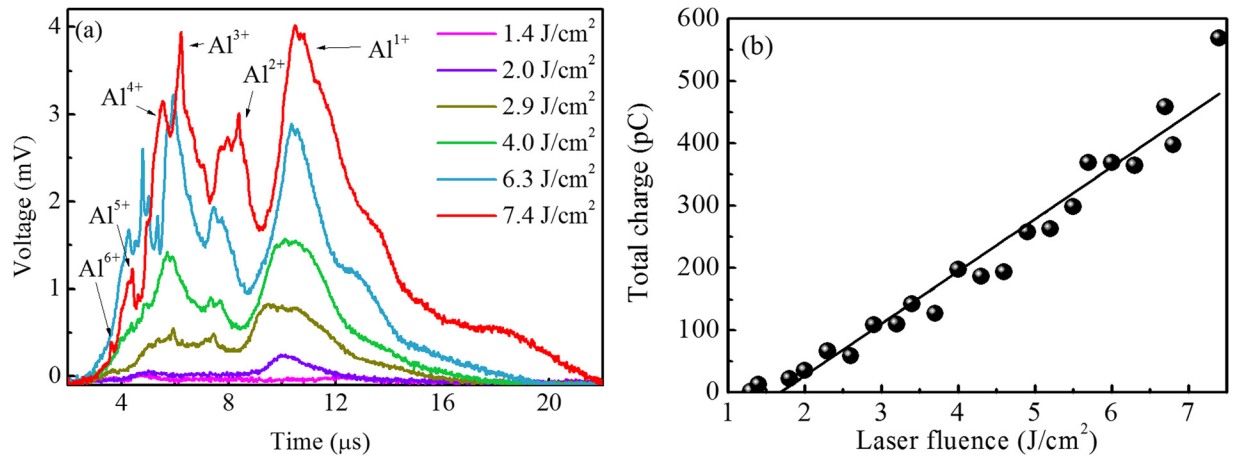
FIG. 5. (a) TOF spectrum of MCIs for laser fluence variation from 1.4 to 7.4 J/cm^2, (b) total charge generation as a function of laser fluence. The accelerating voltage applied to the target was 5 kV.

the vital role.[30] For a metal such as Al, the nonequilibium electrons carry the energy from the optical penetration depth to a deeper region under the surface. For femtosecond laser ablation of Al, low laser fluences produce relatively low hot electron density and the laser energy is mainly deposited in the shallow region defined by the optical penetration depth. With increased laser fluence, the contribution of the heat transport by hot electrons becomes significant resulting in a fast rise in the lattice temperature and the heat affected zone is defined by the hot electron penetration depth. With the increase in the femtosecond laser fluence, explosive evaporation takes place causing less localized energy deposition, which results in the increase in the total ion yield.[30,45]

D. Effect of focal length

The focusing lens was moved longitudinally along the optical axis of the incident laser beam from the focal length position of 324 mm by ±7 mm in 1 mm incremental steps. Throughout this experiment, the voltage applied to the Al target was 5 kV and the laser fluence was at 6.9 J/cm^2 when the target was positioned at the focal length of the lens. The diameter of the laser beam waist changes due to the change in the distance between the Al target surface and the focusing lens, resulting in a reduction in the laser fluence on the Al target surface when the lens position is moved away from the focus.

Fig. 6 shows the effect of changing the focusing lens position on the total Al charge delivered to the FC as a function of the Al target distance from the focal length of the lens. The zero position corresponds to when the Al target is placed at the focal length of the lens (324 mm); positive positions are when the laser is focused in front of the surface, and negative positions are when the laser is focused behind the surface of the target.

It is evident from Fig. 6 that the best focus position for ion production is when the laser is focused 1 mm in front or behind the surface of the target. Moving the position of focus away from the surface of the target increases the spot diameter and reduces the laser fluence on the target. When focusing the laser at a position of ±7 mm away from the surface of the

target, the laser fluence becomes insufficient to ablate the Al target. For ablation of Al using a 120-fs laser pulse with an intensity of 1.5 x 10^{14} W/cm^2, the plume expansion velocity is ~3 × 10^4 ms^{-1}, leading to a length of expanding plume of ~3 nm in front of the target surface.[40] The femtosecond laser pulse does not interact with the expanding plasma as in the case of a nanosecond laser pulse. The absence of interaction of the expanding plasma with the laser pulse makes the ion yield dependence on the focal position similar when the focal spot is before or after the target surface.

The mechanism of material ablation and plasma production by femtosecond laser-matter interaction in vacuum is different from that for nanosecond laser interaction. The duration of interaction of the femtosecond laser pulse with the surface is substantially shorter than the time necessary for the thermal and hydrodynamic mechanisms that dominate during a nanosecond laser pulse.[5,30] We have previously reported on the generation of Al MCI using a Q-switched Nd:YAG laser ($\lambda = 1064$ nm, $\tau \sim 7$ ns, and maximum fluence $F = 38$ J/cm^2) in the same experimental chamber presently used.[23] To remove the same amount of material by laser ablation with a femtosecond pulse requires higher laser intensity than a nanosecond pulse, approximately inversely proportional to the laser pulse duration.[5] For example, to extract a total charge of ~0.7 nC when 5 kV is applied to the
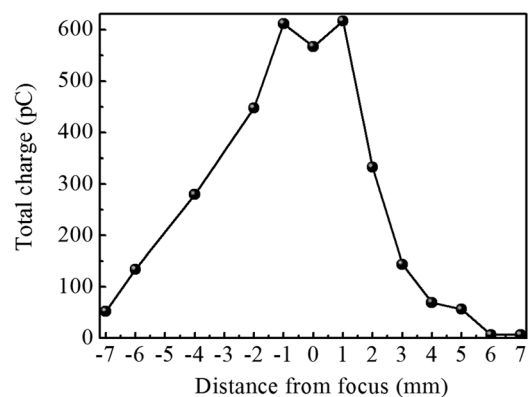

FIG. 6. Al total ion charge detected versus distance from an optical focus of the lens on the target surface.

TABLE I. Comparison of the characteristics of Al MCI generated by femtosecond laser ablation of Al with previously reported nanosecond laser ablation.

Characteristics	Femtosecond laser ($\lambda = 800$ nm)	Nanosecond laser ($\lambda = 1064$ nm)[23]
Ion detection threshold	1.6 J/cm^2	22 J/cm^2
Maximum ion energy gain in the double layer	∼325 eV/charge for laser fluence of 7.6 J/cm^2	∼70 eV/charge for laser fluence of 38 J/cm^2
Maximum charge state achieved	Al^{4+}, Al^{5+}, Al^{6+} for laser fluence of 4.0, 6.3, and 7.6 J/cm^2, respectively	Al^{2+}, Al^{3+}, and Al^{4+} for laser fluence of 25, 28, and 38 J/cm^2, respectively
Ion yield with laser fluence	Increases with fluence up to 7.6 J/cm^2 with no charge saturation observed in this region	Increases with fluence up to 27 J/cm^2 then saturates due to self-absorption
Plasma shielding effect	5 kV accelerating voltage produce Al ions with ∼2.3 keV per charge state	5 kV accelerating voltage produces Al ions with ∼1.8 keV per charge state

target, an intensity of $\sim 8\times10^{13}$ W/cm^2 is required for Al ablation with 100 fs laser pulses, whereas with 7 ns laser pulses an intensity of $\sim 5 \times 10^9$ W/cm^2 is sufficient.[23] Lower plasma shielding effect is observed for femtosecond laser-generated ions compared to when nanosecond pulses are used. This results in the extracted ions gaining more energy from the external electric field when the femtosecond laser is used. The plasma decays faster for the femtosecond laser due to the difference in the energy coupling mechanism and because of the absence of the laser-plasma interaction for the femtosecond laser ablation.[46] Also, at the early stage of the plasma expansion, the femtosecond laser ablated plume is more directed perpendicular to the surface compared to nanosecond ablation resulting in less ion loss due to ion divergence.[46] Higher ablation efficiency is achieved for femtosecond laser ablation due to the lack of interaction between the laser and the plasma compared to nanosecond laser ablation.[47] Table I summarizes results obtained for Al MCI generation by femtosecond and nanosecond laser ablation.

For a laser fluence of 7.6 J/cm^2, the equivalent kT of the ejected ions, as evaluated by deconvolving the TOF signal, is 25 eV when no voltage is applied to the target. However, using a femtosecond Ti:sapphire laser ($\lambda = 800$ nm, $\tau = 100$ fs), which is similar to the one we used, the electron temperature calculated from the optical spectrum was ∼1.4 eV for a laser fluence of 20 J/cm^2.[48] The large difference in the measured plasma temperatures by the two methods is due to the difference in the plasma region probed. The ion TOF contains information on the plasma core zone, where the thermal and Coulomb interactions occur (Knudsen layer). Near the target surface, the plasma density of the inner core is comparable to solid density and the plasma temperature is expected to be much higher than that for the external zone of the expanding plasma.[36] Optical spectroscopy probes the electron temperature of the external zone of the plasma, where lower plasma densities and temperatures are expected. The outer zone of the plasma is formed by the colder neutral and ions of lower charge. Also, the decrease in the temperature in the outer zone is due to the conversion of the thermal energy into kinetic energy with the plasma attaining its maximum expansion velocity.[49]

IV. CONCLUSIONS

Ablation of Al target with 800 nm, 100 fs laser pulse of intensity 10^{13}–10^{14} W/cm^2 is used to generate Al ions. Production of Al ions up to Al^{6+} is observed. The energy distributions of the ejected ions are fitted to an SCB distribution. From this fit, the equivalent plasma ion temperature is found to increase from 25 to 40 eV when an external accelerating voltage of 5 kV is applied to the target setting an electric field in the plasma expansion region. Along the direction normal to target, the ion energy depends on the sum of $E_T + E_K + zE_c + zE_{eff}$, where z is the charge state, indicating that ions are subjected to a Coulomb acceleration proportional to their charge state by the electric field generated in the plasma-vacuum interface of the expanding plume. For higher charge state ions, the Coulomb contribution to the ion velocity is much higher than the thermal ion velocity. For an accelerating voltage of 5 kV, optimal conditions for Al MCI production occur when the Al target surface is positioned ± 1 mm about the focal length of the lens. Plasma shielding and secondary ion generation in the target-to-extraction grid region result in ion energies less than the voltage applied to the target. The laser fluence threshold for Al ion detection with the femtosecond laser was determined to be 1.6 J/cm^2. Comparison of Al ion generation by the ∼100 fs laser pulses to that previously reported with ∼7 ns laser pulses shows that the femtosecond laser has a significantly lower threshold for ion detection and results in a higher ion charge state and ion acceleration, with up to Al^{6+} detected at 7.6 J/cm^2 with 2.3 keV per charge state for the femtosecond laser, while only Al^{4+} with 1.8 keV per charge state is detected at a fluence of 38 J/cm^2 for the nanosecond laser.

[1]J. D. Gillaspy, J. M. Pomeroy, A. C. Perrella, and H. Grube, J. Phys. Conf. Ser. **58**, 451 (2007).
[2]S. Amoruso, M. Armenante, V. Berardi, R. Bruzzese, and N. Spinelli, Appl. Phys. A **65**, 265 (1997).
[3]R. E. Russo, X. Mao, J. J. Gonzalez, V. Zorba, and J. Yoo, *Laser Ablation in Analytical Chemistry* (ACS Publications, 2013).
[4]S. A. Irimiciuc, S. Gurlui, G. Bulai, P. Nica, M. Agop, and C. Focsa, "Langmuir probe investigation of transient plasmas generated by femtosecond laser ablation of several metals: Influence of the target physical properties on the plume dynamics," Appl. Surf. Sci. (published online).
[5]E. Gamaly, A. Rode, B. Luther-Davies, and V. Tikhonchuk, Phys. Plasmas **9**, 949 (2002).
[6]H. E. Elsayed-Ali, T. B. Norris, M. A. Pessot, and G. A. Mourou, Phys. Rev. Lett. **58**, 1212 (1987).
[7]J. Aguilera and C. Aragon, Appl. Phys. A **69**, S475 (1999).
[8]T. Mościcki, J. Hoffman, and Z. Szymański, Arch. Mech. **63**, 99 (2011).
[9]N. M. Bulgakova, A. V. Bulgakov, and O. F. Bobrenok, Phys. Rev. E **62**, 5624 (2000).

[10]V. Nassisi, A. Pedone, and A. Rainò, Nucl. Instrum. Methods B **188**, 267 (2002).

[11]P. Yeates, J. T. Costello, and E. T. Kennedy, Rev. Sci. Instrum. **81**, 043305 (2010).

[12]W. MG. Ibrahim, H. E. Elsayed-Ali, C. E. Bonner, and M. Shinn, Int. J. Heat Mass Transfer **47**, 2261 (2004).

[13]J. Chen, I. V. Tomov, H. E. Elsayed-Ali, and P. M. Rentzepis, Chem. Phys. Lett. **419**, 374 (2006).

[14]X. Liu, D. Du, and G. Mourou, IEEE J. Quantum Electron. **33**, 1706 (1997).

[15]S. Musazzi and U. Perini, "Laser-induced breakdown spectroscopy," in *Theory and Applications* (Springer, 2014).

[16]S. S. Harilal, J. R. Freeman, P. K. Diwakar, and A. Hassanein, "Femtosecond laser ablation: Fundamentals and applications," in *Laser-Induced Breakdown Spectroscopy* (Springer, Berlin Heidelberg, 2014).

[17]K. K. Anoop, S. S. Harilal, R. Philip, R. Bruzzese, and S. Amoruso, J. Appl. Phys. **120**, 185901 (2016).

[18]T. J. Kelly, T. Butler, N. Walsh, P. Hayden, and J. T. Costello, Phys. Plasmas **22**, 123112 (2015).

[19]T. O. N. Y. Donnelly, J. G. Lunney, S. Amoruso, R. Bruzzese, X. Wang, and X. Ni, J. Appl. Phys. **108**, 043309 (2010).

[20]V. Gordienko, I. Lachko, A. Rusanov, A. Savel'Ev, D. Uryupina, and R. Volkov, Appl. Phys. B **80**, 733 (2005).

[21]Z. Zhang, P. A. VanRompay, J. A. Nees, and P. P. Pronko, J. Appl. Phys. **92**, 2867 (2002).

[22]O. Chutko, V. Gordienko, I. Lachko, B. Mar'in, A. Savel'ev, and R. Volkov, Appl. Phys. B **77**, 831 (2003).

[23]M. H. A. Shaim and H. E. Elsayed-Ali, Nucl. Instrum. Methods Phys. Res. B **356–357**, 75 (2015).

[24]M. H. A. Shaim and H. E. Elsayed-Ali, Rev. Sci. Instrum. **86**, 073304 (2015).

[25]M. H. A. Shaim, M. M. Rahman, O. Balki, A. Sarkissian, M. L. Korwin-Pawlowski, and H. E. Elsayed-Ali, Vacuum **137**, 14 (2017).

[26]H. A. Sakaue, K. Hosaka, H. Tawara, I. Yamada, N. Nakamura, S. Ohtani, A. Danjo, M. Kimura, A. Matumoto, M. Sakurai, and M. Yoshino, J. Plasma Fusion Res. Ser. **7**, 195 (2006).

[27]H. Ryufuku and T. Watanabe, Phys. Rev. A **20**, 1828 (1979).

[28]D. Crandall, R. Phaneuf, and F. Meyer, Phys. Rev. A **19**, 504 (1979).

[29]J. Krása, K. Jungwirth, S. Gammino, E. Krouský, L. Láska, A. Lorusso, V. Nassisi, M. Pfeifer, K. Rohelna, L. Torrisi, and J. Ullschmied, Vacuum **83**, 180 (2008).

[30]M. Ye and C. P. Grigoropoulos, J. Appl. Phys. **89**, 5183 (2001).

[31]S. S. Harilal, B. O'shay, M. S. Tillack, and M. V. Mathew, J. Appl. Phys. **98**, 013306 (2005).

[32]B. Verhoff, S. S. Harilal, J. R. Freeman, P. K. Diwakar, and A. Hassanein, J. Appl. Phys. **112**, 093303 (2012).

[33]D. Grojo, J. Hermann, and A. Perrone, J. Appl. Phys. **97**, 063306 (2005).

[34]R. Kelly and R. Dreyfus, Surf. Sci. **198**, 263 (1988).

[35]A. Miotello and R. Kelly, Appl. Sur. Sci. **138–139**, 44 (1999).

[36]F. Caridi, L. Torrisi, and L. Giuffrida, Nucl. Instrum. Methods Phys. Res. B **268**, 499 (2010).

[37]A. Lorussoa, J. Krása, K. Rohlena, V. Nassisi, F. Belloni, and D. Doria, Appl. Phys. Lett. **86**, 081501 (2005).

[38]J. I. Apinániz, B. Sierra, R. Martíńez, A. Longarte, C. Redondo, and F. Castano, J. Phys. Chem. C **112**, 16556 (2008).

[39]R. Teghil, L. d'Alessio, A. Santagata, M. Zaccagnino, D. Ferro, and D. Sordelet, Appl. Surf. Sci. **210**, 307 (2003).

[40]Y. Okano, K. Oguri, T. Nishikawa, and H. Nakano, Appl. Phys. Lett. **89**, 221502 (2006).

[41]B. Verhoff, S. Harilal, and A. Hassanein, J. Appl. Phys. **111**, 123304 (2012).

[42]L. Torrisi, S. Gammino, L. Andò, and L. Laska, J. Appl. Phys. **91**, 4685 (2002).

[43]F. F. Chen, Phys. Fluids **25**, 2385 (1982).

[44]K. Yamada, T. Tetsuka, and Y. Deguchi, J. Appl. Phys. **69**, 6962 (1991).

[45]S. Nolte, C. Momma, H. Jacobs, A. Tünnermann, B. N. Chichkov, B. Wellegehausen, and H. Welling, JOSA B **14**, 2716 (1997).

[46]X. Zeng, X. Mao, R. Greif, and R. Russo, Appl. Phys. A **80**, 237 (2005).

[47]A. Semerok, C. Chaléard, V. Detalle, J.-L. Lacour, P. Mauchien, P. Meynadier, C. Nouvellon, B. Salle, P. Palianov, M. Perdrix, and G. Petite, Appl. Surf. Sci. **138–139**, 311 (1999).

[48]B. Le Drogoff, J. Margot, M. Chaker, M. Sabsabi, O. Barthelemy, T. W. Johnston, S. Laville, F. Vidal, and Y. Von Kaenel, Spectrochim. Acta Part B **56**, 987 (2001).

[49]G. Abdellatif and H. Imam, Spectrochim. Acta B **57**, 1155 (2002).